catalysts

MDPI

Article

Excellent Photoelectro-Catalytic Performance of In_2S_3/NiFe-LDH Prepared by a Two-Step Method

Xiaona Liu [1,2,3,*,†], Zhenzhen Li [1,†], Wenxia Liu [1,*], Huili Wang [1], Zhaoping Song [1,3], Dehai Yu [1] and Guodong Li [1]

[1] Key Laboratory of Pulp and Paper Science & Technology of Ministry of Education, State Key Laboratory of Biobased Material and Green Papermaking, Faculty of Light Industry, Qilu University of Technology, Shandong Academy of Sciences, Jinan 250353, China; 18364196285@163.com (Z.L.); zsong@qlu.edu.cn (Z.S.); yudehai@qlu.edu.cn (D.Y.); lgd@qlu.edu.cn (G.L.)
[2] Shandong Environmental Protection Development Group Co., Ltd., Jinan 250101, China
[3] National Forestry and Grassland Administration Key Laboratory of Plant Fiber Functional Materials, Fuzhou 350108, China
* Correspondence: lxn511944@qlu.edu.cn (X.L.); liuwenxia@qlu.edu.cn (W.L.)
† These authors contributed equally to this work.

Abstract: In this work, we synthesize hierarchical In_2S_3/NiFe-layered double hydroxide (In_2S_3/NiFe-LDH) nanoarrays on an F-doped SnO_2 glass substrate via a two-step method, which the In_2S_3 electrode film was firstly prepared using chemical bath deposition on F-doped SnO_2 glass substrate, and then the layered NiFe-LDH was deposited on In_2S_3 electrode film by hydrothermal synthesis. The two-component photoanode In_2S_3/NiFe-LDH exhibits significantly enhanced photoelectrochemical properties compared with the In_2S_3 single-component; due to that, the NiFe-LDH nanosheets depositing on the surface of In_2S_3 nanocrystal can reduce the accumulation of photogenic holes, facilitate the separation of photogenerated charge carriers, and enhance the light response and absorption. After being decorated with the NiFe-LDH nanosheets, the In_2S_3/NiFe-LDH photoanode displays a lower onset potential of 0.06 V and an enhanced photocurrent density as high as 0.30 $mA \cdot cm^{-2}$ at the potential of 1.0 V (vs. RHE). Furthermore, it also displays a 90% degradation rate of xylose oxidizing into xylose acid in 3 h under UV light. This work provides a promising approach for designing new heterojunctions applied to biomass degradation.

Keywords: photoelectrocatalysis; In_2S_3/NiFe-LDH; hierarchical; oxidation of xylose; biomass degradation

check for updates

Citation: Liu, X.; Li, Z.; Liu, W.; Wang, H.; Song, Z.; Yu, D.; Li, G. Excellent Photoelectro-Catalytic Performance of In_2S_3/NiFe-LDH Prepared by a Two-Step Method. *Catalysts* **2024**, *14*, 230. https://doi.org/10.3390/catal14040230

Academic Editor: Enric Brillas

Received: 1 March 2024
Revised: 22 March 2024
Accepted: 27 March 2024
Published: 29 March 2024

Copyright: © 2024 by the authors. Licensee MDPI, Basel, Switzerland. This article is an open access article distributed under the terms and conditions of the Creative Commons Attribution (CC BY) license (https://creativecommons.org/licenses/by/4.0/).

1. Introduction

The direct conversion of solar energy into chemical energy using semiconductor photoelectrodes has drawn a lot of attention for many decades, particularly in the removal of organic pollutants in water via photocatalysis technology [1–7]. Photocatalysis was defined as a process in which the photocatalyst absorbs light energy and creates the photogenerated electrons and holes that participate in redox reactions, thus achieving the purpose of purifying pollutants, synthesis, and transformation of substances [8–10]. Photoelectrocatalytic methods, combining electrochemical and photocatalysis technologies, have recently raised great interest due to their high efficiency and low cost in removing persistent pollutants in wastewater [11,12]. The photoelectrocatalysis under the action of an electric field inside the semiconductor can further promote the separation of photogenerated carriers, thereby improving the catalytic oxidative degradation efficiency [11,12]. The photocatalytic reaction is a pair of simple conjugated redox reactions in which the role of oxygen is very important because oxygen acts as a receptor for photogenerated electrons and can restrain the recombination of photo-induced carriers [11,12]. The photoelectrocatalytic method of applying an electric field can cause the oxidation reaction and the reduction reaction to occur in different places. The reduction reaction can be either an oxygen reduction in a

solution or a hydrogen evolution reaction, which is different from the usual photocatalytic system. However, almost all photoelectrocatalytic degradation studies have been limited to the oxidation of photogenerated holes [13,14] and often neglected the photoreduction electrons during oxidative degradation. Up to now, several photocatalysts with outstanding properties have been found [15], such as titanium dioxide (TiO_2) [16] and ZnO [17] in the UV spectral range and WO_3 [18], CdS [19], graphene-based hybrid semiconductors, and In_2S_3 in the visible range.

Among various photocatalysts reported, indium sulfide (In_2S_3), due to its low toxicity, high carrier mobility, and stability at ambient conditions, has attracted special interest and been considered a promising candidate for optoelectronic and photovoltaic applications [20]. Although In_2S_3 is an ideal photoanode light absorber, the charge separation efficiency still needs to be improved. In order to efficiently utilize solar energy, improve the separation of photo-induced carriers, and promote the redox reactions, there are many approaches, including engineering the electronic structure by doping metal or nonmetal elements [21,22], designing nanostructure of the photoanodic surfaces [23], and constructing heterojunction composite by coupling two energy level-matching semiconductors [24–26]. IrO_2 and RuO_2 were once employed as catalysts to improve photocatalytic activity, but this strategy is limited due to its high cost [27]. Layered double hydroxide (LDH) material is a kind of anionic clay, with the layered framework consisting of the divalent and trivalent metal cations uniformly distributing and the anions intercalating [28,29]. Therefore, transition metal (oxy)hydroxides, such as $Ni(OH)_2$ [30], CoFe layered double hydroxide (CoFe-LDH), and NiFe-layered double hydroxide (NiFe-LDH) [31–34], have been widely applied due to their evident enhancement in the water oxidation efficiency by alleviating photogenerated holes accumulation and enhancing oxygen evolution kinetics.

Xylose, an abundant pentose sugar present in lignocellulosic plant material, is currently considered a potential primary source for ethanol or xylitol production used in many fields, such as the synthesis of various biodegradable chemicals, chelating agents, additives for cement, concrete, food, and pharmaceutical, etc. [35–39]. Therefore, scientists have developed many different chemical and biological methods attempting to oxidize xylose into xylose acid and other chemicals. Mervi Toivari and his team reported the metabolic engineering of saccharomyces cerevisiae for the bioconversion of D-xylose to D-xylonate, while others achieved xylonic acid from xylose via using bacteria [40]. Chen et al. designed a TiO_2/Ti_3C_2(TT) photocatalyst for the oxidation of xylose to D-xylonic acid under ambient conditions, exhibiting 64.2% of D-xylonic acid yield with excellent stability [41]. Li et al. reported that ZnS@Bi_2S_3 nanosheets prepared by one-step controllable, which were used for the highly selective oxidation of biomass-derived monosaccharides to produce value-added sugar acids [42]. The microbial conversion of xylose has good selectivity; however, the conversion efficiency is still low, and it is difficult to separate the microbes and control the generation of by-products, so it is of great significance to seek new approaches to settle these problems. Now, there are two chemical methods for the oxidation of xylose into xylonic acid. One is that xylose is oxidized in aqueous media with the catalysts of precious metal Pd or Pt supported on Mg, γ-Al_2O_3, carbon black, etc., in the presence of oxygen, air, and hydrogen peroxide [43]. Mirescu and Prüe reported that the selectivity of 4.6% Pd/Al_2O_3 catalyst reached 99% for the oxidation of xylose and that 0.45% Au/TiO_2 catalyst was higher than 99.5% under the same conditions [44]. The other method is electrochemical oxidation, which does not require the addition of additional oxidants and can be activated on solids. The reaction activity can be controlled precisely by changing the structure/composition of the catalyst, and the reaction selectivity can be improved by adjusting the anode potential (battery voltage) to control the adsorption/activation of the water and sugar on the surface of the catalyst [43,45–47]. However, few studies have been conducted on this presently, and only platinum and gold have been investigated extensively, ascribing to their good activity in electrochemical reactions.

Based on the above, we propose an electrochemical oxidation-like method, a photoelectrochemical method, applying for the oxidation of xylose into xylose acid in this work.

The first step is to choose the appropriate photocatalytic material. Nanostructured semiconductor materials prepared on fluorine-doped tin oxide (FTO) or fluorine-doped indium tin oxide (FITO) substrates possess higher adhesion and electron transfer efficiency [48]. Moreover, layered double hydroxide (LDH) directly hydrothermally grown on semiconductor photocatalysts also exhibits better adsorption and higher activity. In this work, the hierarchical In_2S_3/NiFe-layered double hydroxide (In_2S_3/NiFe-LDH) nanoarrays on an F-doped SnO_2 glass substrate via a two-step method was synthesized, whereby the In_2S_3 electrode film was firstly prepared using chemical bath deposition on F-doped SnO_2 glass substrate, and then the layered NiFe-LDH was deposited on In_2S_3 electrode film by hydrothermal synthesis. The two-component photoanode In_2S_3/NiFe-LDH exhibits significantly enhanced photoelectrochemical properties compared with the In_2S_3 single-component; due to that, the NiFe-LDH nanosheets depositing on the surface of In_2S_3 nanocrystal can reduce the accumulation of photogenic holes, facilitate the separation of photogenerated charge carriers, and enhance the light response and absorption. After being decorated with the NiFe-LDH nanosheets, the In_2S_3/NiFe-LDH photoanode displays a lower onset potential of 0.06 V and an enhanced photocurrent density as high as 0.30 $mA \cdot cm^{-2}$ at the potential of 1.0 V (vs. RHE). Furthermore, the prepared In_2S_3/NiFe-LDH semiconductor material was used for photoelectrodes to degrade xylose, and it displayed excellent degradation performance under both ultraviolet light and visible light, with an oxidation rate higher than 90% within 3 h under UV light, indicating that the prepared In_2S_3/NiFe-LDH semiconductor material can successfully oxidize xylose into xylose acid. This work provides a promising approach for designing new heterojunctions to apply to biomass degradation.

2. Results and Discussion

2.1. XRD Structural Characterization

The XRD patterns of the pristine In_2S_3 and In_2S_3/NiFe-LDH are shown in Figure 1. All the diffraction peaks in Figure 1a are in good consistency with the standard data of the cubic structure In_2S_3 (JCPDS no.32-0456) [49], which is in accordance with SEM, and the sharp diffraction peaks imply that the In_2S_3 sample was highly crystallized. As is shown in Figure 1b, there exist the diffraction peaks not only of cubic structure In_2S_3, denoted by dots, but also of NiFe-LDH (JCPDS no.38-0715) [29], denoted by rhombuses, which indicates that the composite of In_2S_3 and NiFe-LDH was successfully synthesized using the two-step method. No characteristic peaks of any impurities were detected.

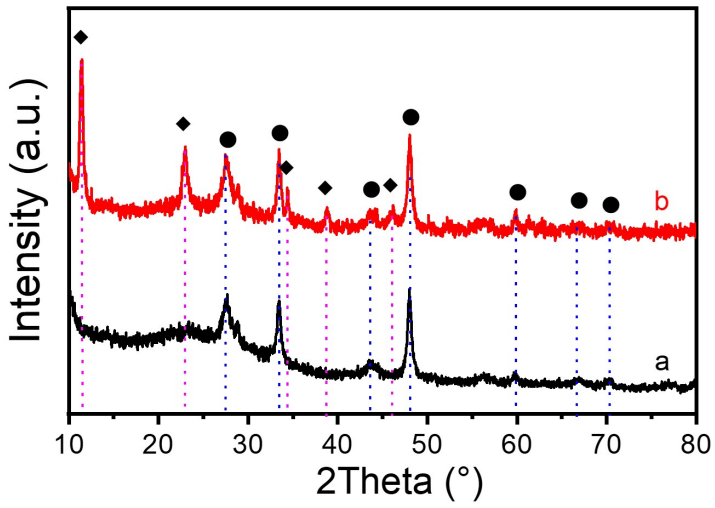


Figure 1. XRD patterns of (a) In_2S_3 and (b) In_2S_3/NiFe-LDH. Insets: Peaks due to In_2S_3 (●) and NiFe-LDH (◆).

2.2. SEM and TEM Morphology Characterization

The morphologies of pristine In_2S_3, NiFe-LDH, and In_2S_3/NiFe-LDH were observed using SEM and TEM. In Figure 2a, the cubes of In_2S_3 are clearly observed, which further proves the cubic phase of In_2S_3. Figure 2b,c shows the morphology of the synthesized Ni-Fe hydrotalcite and In_2S_3/NiFe-LDH, respectively. The sample was rapidly dried in an oven at a high temperature, resulting in slight damage and cracking of the NiFe-LDH on the surface layer, and thus the double-layered material deposited on the FTO can be observed in Figure 2c. It can clearly be seen that the grain size of In_2S_3 is obviously larger than that of NiFe-LDH in Figure 2a,b, and there are thin NiFe-LDH films grown uniformly on the In_2S_3 displayed in Figure 2e. At the same time, in order to observe the growth thickness of In_2S_3, we photographed the cross-section of the material. It can be seen from Figure 2d that the thickness is about 1 µm. The synthesized In_2S_3/NiFe-LDH is further characterized by TEM, EDX, and mapping. Figure 2e exhibits the cubic shape of synthetic In_2S_3 and the layered structure of NiFe-LDH. The HRTEM images in Figure 2f of the In_2S_3/NiFe-LDH reveal that the fringe spacing of 0.319 nm and 0.257 nm agree well with the spacing of the lattice plane (311) of In_2S_3 and lattice plane (012) of NiFe-LDH, respectively, indicating the formation of NiFe-LDH on the surface of In_2S_3. The EDS elemental analysis in Figure 2g displays the presence of In, S, Ni, Fe, and O elements and uniform signals of In, S, Ni, Fe, and O elements in the SEM-EDS elemental mapping images (as shown in Figure 2h–l) demonstrates the homogeneous distribution of NiFe-LDH on the In_2S_3 surface. These results suggest that In_2S_3 can be well decorated with the NiFe-LDH, which is favorable for facilitating the charge transfer between the In_2S_3 and NiFe-LDH.

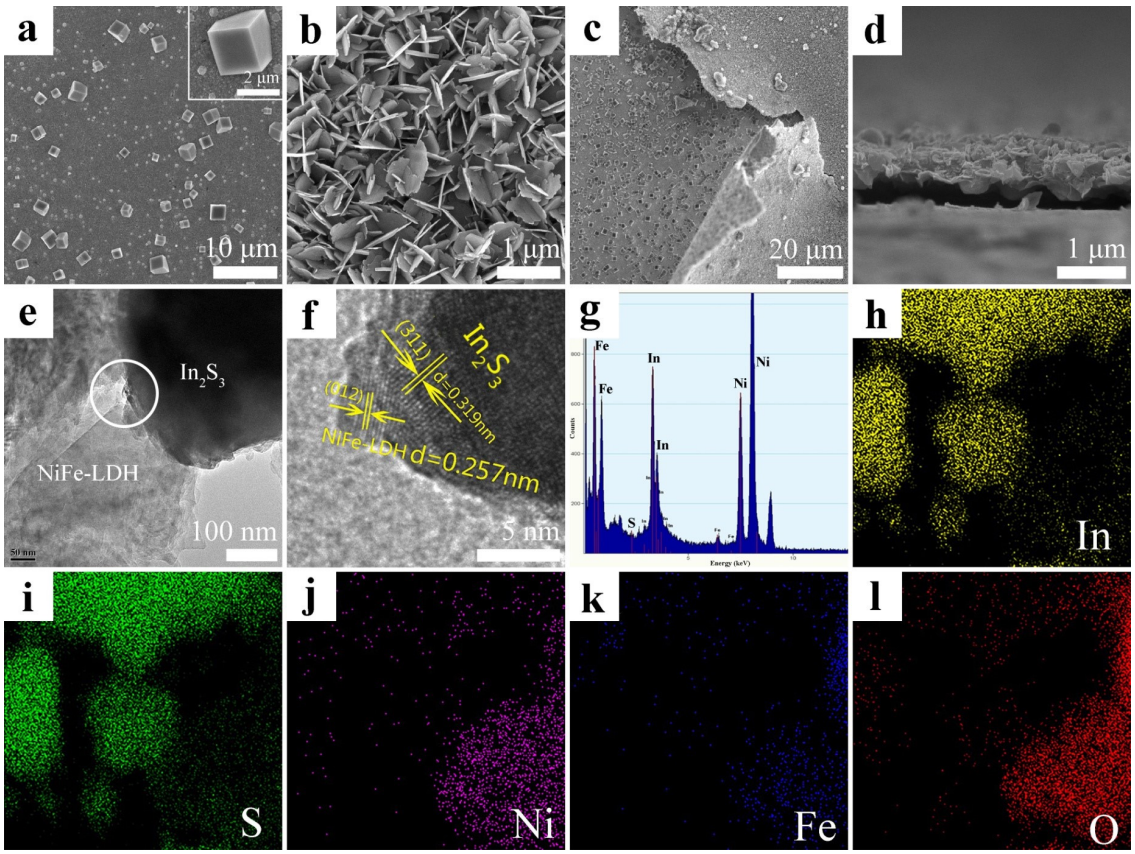


Figure 2. SEM images of the In_2S_3 (**a**), NiFe-LDH (**b**), and In_2S_3/NiFe-LDH (**c**,**d**). HRTEM images of In_2S_3/NiFe-LDH (**e**,**f**). Energy dispersive spectroscopy (EDS) spectra (**g**) and mapping (**h**–**l**) of In_2S_3/NiFe-LDH.

2.3. XPS Characterization

The surface chemical composition and valence states of the as-prepared In_2S_3/NiFe-LDH were investigated using X-ray photoelectron spectrometry (XPS) measurements, as shown in Figure 3, and the binding energies obtained in the XPS analysis were corrected for specimen charging by reference to a C 1s value of 284.6 eV. Figure 3a provides the general survey spectrum of In_2S_3/NiFe-LDH, which demonstrates the existence of In, S, Ni, Fe, O, and C elements in the sample. The observed C peak at 284.6 eV may be ascribed to an adventitious carbon-based contaminant, which is used to calibrate all of the binding energies, while the O element detected in XPS spectra could be oxygen from Ni- and Fe-hydroxides. The XPS spectrum of the In_2S_3 sample is similar and consistent with the typical In_2S_3 spectrum reported in the literature [50]. The XPS spectrum of the In 3d region is displayed in Figure 3b, consisting of two characteristic peaks with binding energies of 445.2 eV and 452.8 eV, which correspond to the signals from doublets of In $3d_{5/2}$ and In $3d_{3/2}$ in the trivalent oxidation state, respectively. The peaks, located at 161.8 and 163.0 eV, as shown in Figure 3c, could be assigned to the −2 valence state of sulfur for the S $2p_{3/2}$ and S $2p_{1/2}$, respectively [51]. Figure 3d shows the high-resolution XPS peaks of Ni element, exhibiting the Ni 2p spectrum with two peaks at the binding energies of 855.7 and 873.4 eV, which can be assigned to $2p_{3/2}$ and $2p_{1/2}$ peaks in NiFe-LDH, respectively. The Fe 2p spectrum in Figure 3e shows two peaks at 704.1 and 724.2 eV, which are assigned to Fe $2p_{3/2}$ and Fe $2p_{1/2}$ in NiFe-LDH, respectively [52]. As displayed in Figure 3f, the characteristic peak of O1s around 530.5 eV comes from the overlapping contributions of oxide ions Gaussian fitted into three peaks: at 530.3, 531.0, and 531.7 eV, which were contributed to O^{2-} species, chemisorbed activity (O_2^{2-} and O^-), and adsorbed molecular water, respectively [53,54]. The XPS results prove that the formation of NiFe-LDH in the In_2S_3/NiFe-LDH composite occurs, which is in good accordance with the results of the XRD, SEM, and HRTEM analyses.

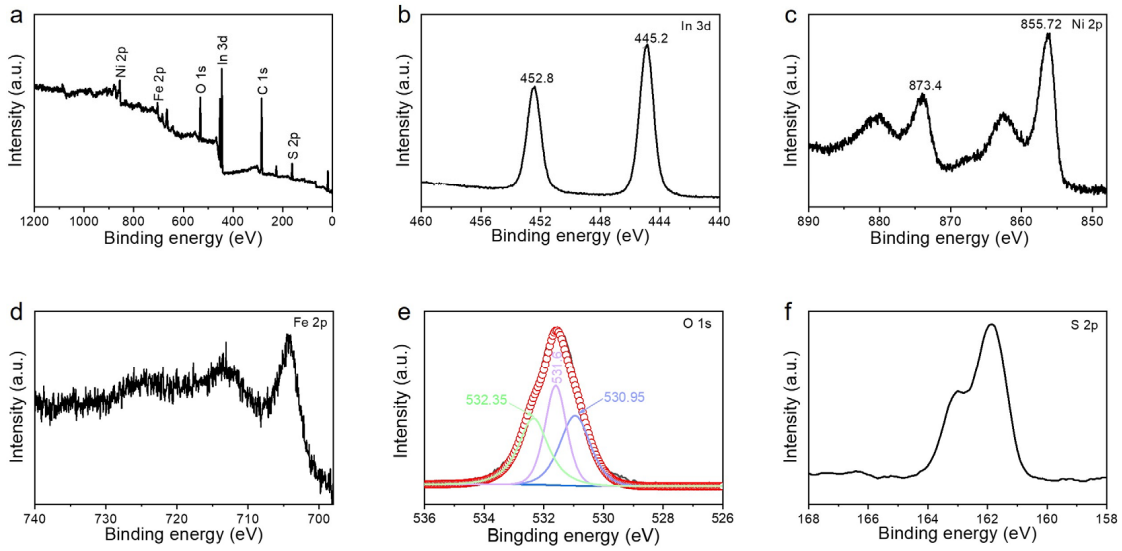


Figure 3. (**a**) XPS–fully scanned spectra, (**b**) In 3d spectra, (**c**) S 2p spectra, (**d**) Ni 2p spectra, (**e**) Fe 2p spectra, and (**f**) O 1s XPS spectra.

2.4. UV–Vis Absorption Spectra

The UV–vis absorption spectra in Figure 4 were used to investigate the optical properties of In_2S_3, NiFe, and In_2S_3/NiFe-LDH. All the samples were scraped from the FTO conductive glass for the convenience of testing. It is obvious that the In_2S_3 sample has significant absorption in a wavelength of less than 630 nm and weak absorption in a wavelength greater than 630 nm. After being decorated with NiFe-LDH nanosheets, the visible light absorption of In_2S_3/NiFe-LDH increases compared with that of NiFe-LDH, demon-

strating that it has good visible light response ability. The band gap can be calculated by Eg = 1240/λ, where the λ is the optical absorption edge of the semiconductor. The optical absorption edges of In_2S_3 and NiFe are 619 and 780 nm, and their corresponding band gaps are calculated to be 2.00 and 1.59, respectively, in line with the previous reports [55,56].

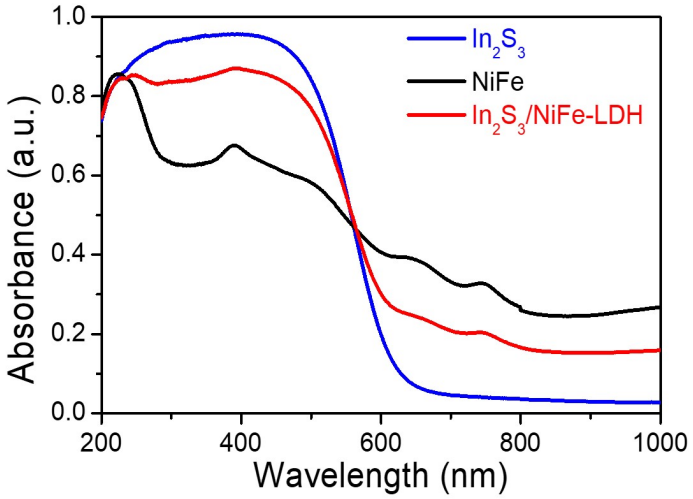


Figure 4. UV–Vis diffuse reflectance spectra of the samples.

2.5. Photoelectrochemical (PEC) Performance

To study the PEC performance of NiFe-LDH nanosheet arrays loaded on the In_2S_3 photoanode, the samples were fabricated as photoanodes with a well-defined area of 1 cm^2. All PEC properties were measured under AM 1.5 G simulated sunlight (100 mW cm^{-2}) in a standard three-electrode electrochemical cell with a Pt foil as the counter electrode, an Ag/AgCl as the reference electrode, and a 0.25 M $NaSO_4$ solution as the electrolyte. According to previous reports [57,58], the tests were measured under the backlight to obtain a better photocurrent, ascribing to the photogenerated electrons having to travel longer distances collected by FTO back contact under front-side illumination. The relationship between current density and voltage of prepared In_2S_3/NiFe-LDH optoelectronic materials was studied by linear scanning voltammetry (LSV). As shown in Figure 5a, the current density of the simple FTO conductive glass sheet is almost zero, and that of the single-layer of In_2S_3 photoelectric material, whose maximum current density is just 0.1 mA/cm^2 in the voltage range of 0–1.0 V, is also relatively small. At the same time, the current density of In_2S_3/NiFe-LDH optoelectronic material increases obviously, about three times higher than that of In_2S_3 at 1.0 V voltage, after the NiFe-LDH nanosheet arrays grown on the surface of In_2S_3, which means that more photo-induced electrons are transferred to the opposite electrode via the external circuit In_2S_3/NiFe-LDH nanomaterials. The Mott–Schottky test can determine the type of semiconductor, the carrier concentration, and the flat band potential. Therefore, in order to evaluate the conductor types of the synthesized In_2S_3/NiFe-LDH optoelectronic materials and to further study the charge separation process on the electronic properties, the Mott–Schottky curves of In_2S_3/NiFe-LDH optoelectronic materials were tested under dark conditions. Three frequencies of the In_2S_3/NiFe-LDH optoelectronic materials were tested using the Mott–Schottky test to explore the influence of different frequencies on the materials. As shown in Figure 5b, all curves show positive slopes, indicating that the In_2S_3/NiFe-LDH are n-type semiconductors, and the space charge layer differential capacitance of the semiconductor is different at different frequencies under the same electric potential [59].

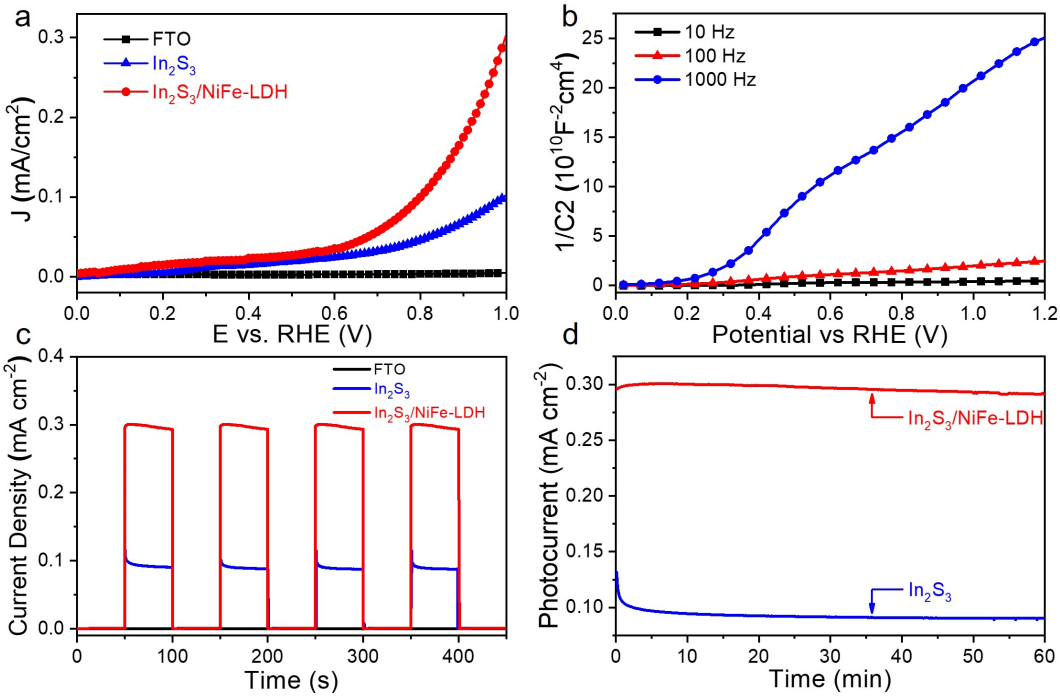


Figure 5. Effect of NiFe-LDH on PEC performance of the In_2S_3/NiFe-LDH photoanode. (**a**) The LSV curves, (**b**) Mott−Schottky plots of In_2S_3/NiFe-LDH, (**c**) I−t curves at a potential of 1.0 V vs. RHE under AM 1.5 global irradiation in a 0.25 M Na_2SO_4 solution, (**d**) time current stability a potential of 1.0 V vs. RHE under AM 1.5 global irradiation in a 0.25 M Na_2SO_4 solution.

The transient current responses of In_2S_3 and In_2S_3/NiFe-LDH photoelectric materials were measured using the chronocurrent method shown in Figure 5c. AM 1.5 G simulated sunlight was used to illuminate optoelectronic material, and the light source was switched every 50 s. When the light source is switched on, the transient current of In_2S_3/NiFe-LDH optoelectronic material can reach 0.3 mA/cm^2, while that of In_2S_3 optoelectronic material can only reach 0.1 mA/cm^2 in four cycles. Another important performance of PEC battery applications is photochemical stability. Figure 5d shows the photocurrent stability (relative to the time curve) of In_2S_3 and In_2S_3/NiFe-LDH optoelectronic materials under AM 1.5 G simulated sunlight. In Figure 5d, In_2S_3 and In_2S_3/NiFe-LDH photoelectricity materials still kept good stability with different photocurrent after 1 h irradiation, indicating that the In_2S_3/NiFe-LDH photoelectricity materials not only have high photoelectricity but also have good photostability and chemical stability in electrolyte solution (SO_3^{2-}).

In order to further investigate the influence of heterojunction on the charge separation process and electronic properties, the electrochemical impedance spectroscopy (EIS) of In_2S_3 and In_2S_3/NiFe-LDH photoelectrodes was measured in Figure 6. The Nyquist diagram obtained by In_2S_3 and In_2S_3/NiFe-LDH at open circuit potential is shown in Figure 6. The proposed Randles circuit of both In_2S_3 and In_2S_3/NiFe-LDH is in good agreement with the experimental data points (fitting error ~0.01). In addition, the EIS curve of In_2S_3/NiFe-LDH photoanode shows a smaller diameter than that of In_2S_3 photoanode under illumination, meaning that the resistance of In_2S_3/NiFe-LDH electrolyte interface is much smaller than that of the In_2S_3 electrolyte interface [60], which demonstrates that the NiFe-LDH nanosheets can effectively promote the charge transfer between the photoelectrode/electrolyte interface and thus enhance the photoelectric properties of In_2S_3/NiFe-LDH materials.

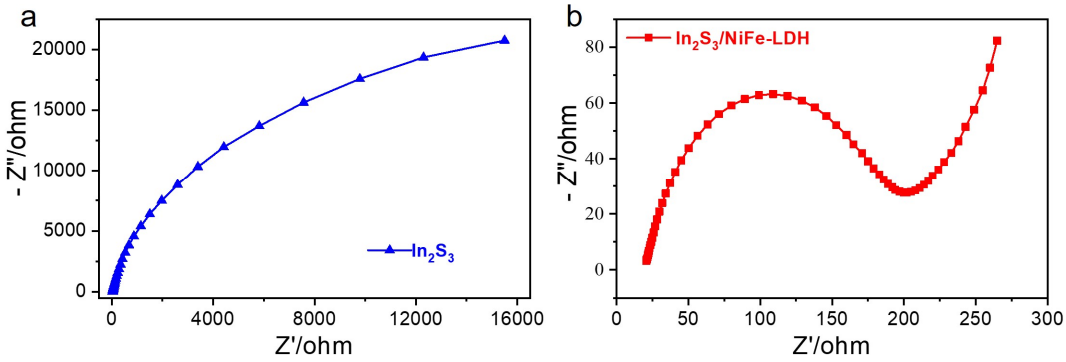


Figure 6. EIS spectra of In_2S_3 (**a**) and In_2S_3/NiFe-LDH (**b**) measured at the open−circuit potential under illumination.

2.6. Photodegradation of Xylose

The redox ability of the In_2S_3/NiFe-LDH material was obtained by the oxidation and degradation of the xylose standard solution. At room temperature, a three-electrode system was used, and the light source was AM 1.5 global irradiation. A 30 mL xylose standard solution and a 30 mL sodium sulfate solution were added to the electrolytic cell, and the xylose standard solution was oxidatively degraded under constant stirring at a constant battery voltage of 0.2 V vs. RHE. During the progress, the hydrogen evolution reaction ($2\ H_2O + 2\ e^- \rightarrow H_2 + 2\ OH^-$) occurred at the cathode, and the oxidation of xylose to xylic acid ($C_5H_{10}O_5 + 3\ OH^- \rightarrow C_5H_9O_6^- + 2\ H_2O + 2\ e^-$) occurred at the anode. The possible photo-induced electron–hole separation processes of samples are shown in Figure 7. The photogenerated electrons on the surface of samples transfer into the conduction band under light illumination. The electrons move quickly to the cathode, and a hydrogen evolution reaction occurs under applied voltage; meanwhile, the xylose oxidizes to xylic acid at the anode. Thus, the photogenerated electrons and holes could be separated effectively. In this way, the recombination of electron–hole pairs can be reduced, resulting in excellent photoelectrocatalytic activity. The residual xylose in electrolytic cells was determined using the phloroglucinol method: the aldehyde group in the lignin reacts with phloroglucinol to form a purple-red substance, which has an absorption peak at 554 nm [61]. Xylose solutions were sampled near the In_2S_3/NiFe-LDH electrode material at given irradiation time intervals of 30 min. After 3 h, the xylose content near the In_2S_3/NiFe-LDH electrode material was significantly reduced.

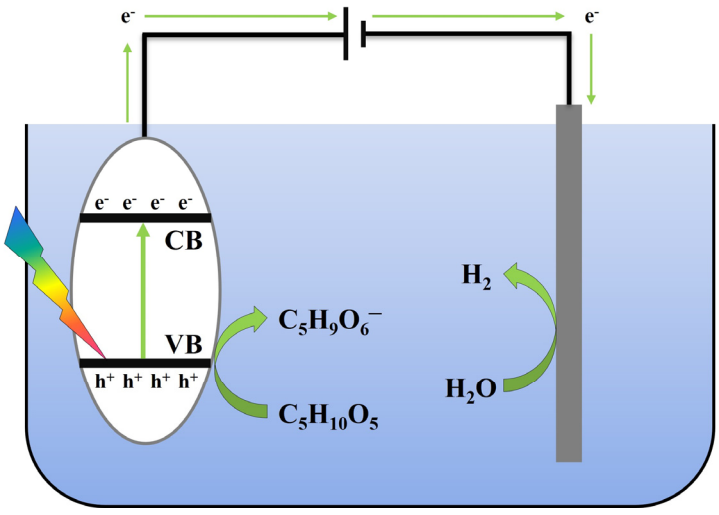


Figure 7. Schematic description of the photoelectrocatalytic mechanism of samples.

The amount of xylose remaining was also measured in the solution every 30 min. Figure 8a reveals the degradation of xylose in the photodegradation solution under UV, Vis, and NIR lights, and the photo-oxidation effect under UV light is the best. The xylose near the In_2S_3/NiFe-LDH electrode material is almost completely degraded, with a degradation rate of over 90% under UV light after 3 h, while the degradation effect of xylose under visible light applied voltage reached about 80%. In addition, the effect of simple voltage on the degradation of xylose was also explored. It is obvious that the simple electrocatalytic degradation of xylose was not very satisfactory, and the degradation rate was about 10% after 3 h. The oxidative degradation of the xylose solution by photoelectric materials under pure illumination was also carried out, as shown in Figure 8b, and the results indicated that the degradation effect of xylose by simple illumination is directly proportional to the effect of photocatalytic degradation of xylose. The effect of applied voltage on the photodegradation of xylose was determined in combination with Figure 8a,b; it can be concluded that the applied voltage can promote the transfer of photogenerated carriers, accelerate the degradation effect, and facilitate the reaction more easily. Figure 8c displays the temporal evolution of the absorbance changes at a time interval of 30 min. During the reaction of photoelectrocatalytic degradation, the residual xylose content was gradually reduced to the wavelength of 554 nm and kept stable ultimately after 3 h.

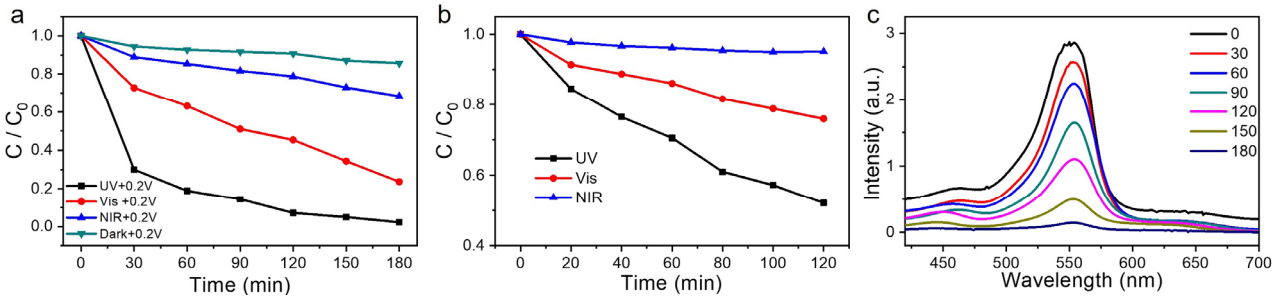


Figure 8. Photodegradation of xylose under (**a**) UV, visible, and NIR lights at 0.2 V and (**b**) UV, visible, and NIR lights, respectively. (**c**) The temporal evolution of the spectra during photoelectrocatalytic degradation of xylose with In_2S_3/NiFe-LDH under UV light.

Finally, the products after the degradation reaction of xylose were also examined. Firstly, the degradation products were purified by distillation and concentrated and freeze-dried. The analysis by ^{1}H NMR of the degradation reaction products was used to confirm the nature of the compounds formed at the anode. Figure 9 provides the ^{1}H NMR spectra for the initial xylose solution before (black curve) and after (red curve) photodegradation normalized with respect to the internal reference, in which the ^{1}H NMR spectrum of the initial xylose solution shows typical signals for xylose in water with several peaks in the 3.0 to 3.6 ppm range; the two doublets at δ = 4.4 ppm and δ = 5.1 ppm are the typical hydrogens on the anomeric carbon of the α and β forms, respectively, and a quadruplet of peaks at δ = 3.75 ppm are attributed to the hydrogen on the carbon next to the anomeric carbon of the β form of xylose [43]. After photodegradation for 3 h, the xylose signal was lowered, and the total amount and position of the peaks in the range of 3.0 to 3.8 ppm changed. Typical peaks belonging to xylogous acid neared δ = 3.8 and δ = 3.9 ppm appeared.

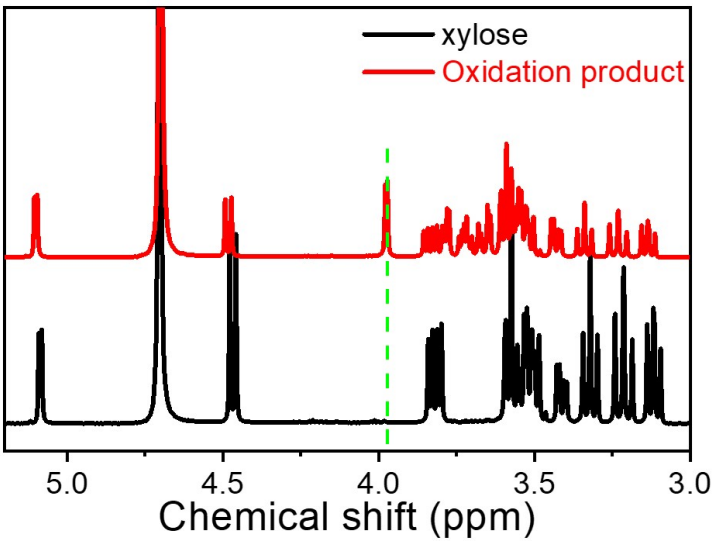


Figure 9. D_2O ^1H NMR of xylose and oxidation product.

3. Materials and Methods

3.1. Materials

All chemicals used in the experiments were of analytical grade and were used as purchased without further purification. $InCl_3$ and $C_5H_{12}O_5$ were purchased from the McLean Reagent. Purified water (18.2 MX cm) for the experiments was attained from a Molecular Lab water purifier. The fluorine-doped tin oxide-coated glass (FTO, Zhuhai Kaivo Optoelectronic Technology Co., Ltd. (Zhuhai, China), <15 X/sq) was first cleaned with a detergent, boiled in a mixed solution of 30% ammonia water, 30% hydrogen peroxide, and ultrapure water for 30 min, then ultrasonically in ultrapure water and pentahydrate ethanol for 15 min, and finally sealed in anhydrous ethanol for later use.

3.2. Synthesis of In_2S_3 Electrodes Film

Firstly, the proper amount of citric acid coordination agent was dissolved in deionized water, and then 0.001 mol $InCl_3$ ($InCl_3$: citric acid = 1:6) was added into the solution continuously to obtain a completely clear and transparent solution, whose pH was about 2. Then, a CH_3CSNH_2 solution ($InCl_3$: CH_3CSNH_2 = 1:4) was slowly added to the above solution and continuously stirred to obtain a transparent precursor solution, whose apparent concentration of In_2S_3 was 0.01 mol/L. Then, the precursor solution was transferred into the reaction vessel, and the pre-treated F-doped SnO_2 glass substrate was also placed in the above solution. Finally, the reaction vessel was kept at 80 °C for 8 h, and then the resultants were purified, cleaned, and dried to obtain an orange indium sulfide film.

3.3. Coating of NiFe-LDH Film on In_2S_3 Electrodes

NiFe-LDH films were grown on In_2S_3 electrodes using the hydrothermal method. Firstly, $Ni(NO_3)_2{\cdot}6H_2O$ (2.4 mmol), $Fe(NO_3)_3{\cdot}9H_2O$ (0.8 mmol), and $CO(NH_2)_2$ were dispersed in 35 mL deionized water, then the above solution with 5 mmol In_2S_3-FTO was transferred into a 50 mL Teflon-lined stainless-steel autoclave, which was sealed and maintained at 120 °C for 12 h. The products were subsequently washed using deionized water/ethanol three times and dried at 80 °C for 2 h.

3.4. Characterization

Powder X-ray diffraction patterns of the samples were collected on a Bruker (Billerica, MA, USA) D8 Advance powder diffractometer operating at 40 kV, 40 mA for Cu Kα radiation (λ = 1.54 Å) using a Cu Kα source, with a scan step of 0.02 and a scan range between 5° and 80°. The surface morphologies of the samples were characterized using scanning electron microscopy (SEM, Hitachi Regulus 8220, Tokyo, Japan) and transmission

electron microscopy (TEM, TF20, Electronics Co., Ltd. Jeol 2100F, Tokyo, Japan). X-ray photoelectron spectra (XPS) were measured using Thermo ESCALAB 250XI (Waltham, MA, USA) with X-ray monochromatization. The C1s peak at 284.8 eV was used as a reference for calibrating the binding energies of all the XPS spectra. The UV–Vis absorption spectra of the synthesized samples were measured using a near-infrared UV–Vis spectrophotometer (Cary (Addison, IL, USA) 5000 UV–Vis–NIR).

3.5. Photoelectrochemical Measurements

All photoanodes were measured as working electrodes by exposing an area of 1 cm^2 on a CHI660A electrochemical workstation. The three-electrode configurations, using Pt foil as counter electrodes and the Ag/AgCl electrode (3.0 M KCl) as a reference electrode, were adopted for photoelectrochemical measurements in a 0.25 M Na_2SO_4 solution. Linear sweep voltammograms (LSV) at a scan rate of 10 mV/s and amperometric i-t curves under chopped light were carried out under AM 1.5 G (100 mW/cm^2) (λ > 420 nm) illumination. Electrochemical impedance spectra (EIS) of In_2S_3/NiFe-LDH were performed in the frequency range of 100 kHz to 0.1 Hz, with an amplitude of 10 mV. Mott–Schottky analysis was carried out in a DC potential range of 0–1.2 V vs. RHE, with an AC potential frequency of 1 kHz under dark conditions. All measured potentials were converted to V vs. RHE (ERHE = $E_{Ag/AgCl}$ + 0.208 + 0.059 pH).

3.6. Photoelectrocatalytic Oxidation of Xylose

The oxidation degradation of xylose was carried out using the synthesized In_2S_3/NiFe-LDH. A 40 mL xylose solution with a concentration of 1 mg/mL and a Na_2SO_4 solution were added into a quartz container. Pt was used as an opposite electrode, Ag/AgCl was used as the reference electrode, and In_2S_3/NiFe-LDH was used as the working electrode. The content of residual xylose in the container was measured every 30 min, and the concentration of residual xylose was measured at 554 nm using a UV–Vis spectrophotometer (Shimadzu, Kyoto, Japan). The xylose solution was distilled and condensed, and the product was detected.

4. Conclusions

In summary, the hierarchical In_2S_3/NiFe-layered double hydroxide (In_2S_3/NiFe-LDH) nanoarrays on an F-doped SnO_2 glass substrate via a facile two-step method were synthesized and investigated. After being decorated with the NiFe-LDH nanosheets, the two-component photoanode In_2S_3/NiFe-LDH exhibited significantly enhanced photoelectrochemical properties compared with the In_2S_3 single-component; due to that, the NiFe-LDH nanosheets depositing on the surface of the In_2S_3 nanocrystal can reduce the accumulation of photogenic holes, facilitate the separation of photogenerated charge carriers, and enhance the light response and absorption. Furthermore, the prepared In_2S_3/NiFe-LDH semiconductor material was used for the photoelectrodes to degrade xylose and displayed excellent degradation performance under both ultraviolet light and visible light, with an oxidation rate higher than 90% within 3 h under UV light, indicating that the prepared In_2S_3/NiFe-LDH semiconductor material can successfully oxidize xylose into xylose acid, as confirmed by ^{1}H NMR. This work provides a promising approach for designing new heterojunctions to apply to biomass degradation.

Author Contributions: Conceptualization, methodology, software, and validation, Z.L.; formal analysis and investigation, Z.L. and X.L.; resources, data curation, X.L. and W.L.; writing—original draft preparation, Z.L. and X.L.; writing—review and editing, X.L. and W.L.; visualization, Z.S. and G.L.; supervision, D.Y.; project administration, H.W. and W.L.; funding acquisition, X.L., H.W. and W.L. All authors have read and agreed to the published version of the manuscript.

Funding: This research was funded by the National Natural Science Foundation of China (No. 22006082 and 52172147), the Natural Science Foundation of Shandong Province (No. ZR2022MB095 and ZR2021MB035), Shandong Province Key Research and Development Program (No. 2021ZDSYS18),

the QUTJBZ Program (No. 2022JBZ01-05), and the Integration Pilot Program of Science, Education, and Industry, and the Talent Scientific Research Project of Qilu University of Technology (No. 2023PY036 and 2023RCKY181), Foundation of State Key Laboratory of Biobased Material and Green Papermaking, Qilu University of Technology (No. GZKF202214, ZZ20210111 and ZZ20210101), Foundation of National Forestry and Grassland Administration Key Laboratory of Plant Fiber Functional Materials (No. 2020KFJJ01).

Data Availability Statement: The data presented in this study are available on request from the corresponding author.

Acknowledgments: This work was financially supported by the Shandong Environmental Protection Development Group Co., Ltd.

Conflicts of Interest: The authors declare that this study received funding from Shandong Environmental Protection Development Group Co., Ltd. The funder was not involved in the study design, collection, analysis, interpretation of data, the writing of this article or the decision to submit it for publication.

References

1. Guan, R.Q.; Cheng, X.Y.; Che, W.L.; Chen, Y.N.; Wu, Z.K.; Shang, Q.K. Synergistic Regulation of Hydrophobicity and Carrier Transport Based on Bipyridine Derivatives to Enhance the Photocatalytic Performance of Defective TiO_2 for Ammonia Synthesis. *ACS Sustain. Chem. Eng.* **2024**, *12*, 4587–4597. [CrossRef]
2. Nozik, A.J. Photoelectrochemistry: Applications to solar energy conversion. *Ann. Rev. Phys. Chem.* **1978**, *29*, 189–222. [CrossRef]
3. Bard, A.J. Photoelectrochemistry and heterogeneous photo-catalysis at semiconductors. *J. Photochem.* **1979**, *10*, 59–75. [CrossRef]
4. Gerischer, H. Solar photoelectrolysis with semiconductor electrodes. In *Solar Energy Conversion*; Springer: Berlin/Heidelberg, Germany, 1979; pp. 115–172.
5. Murphy, A.B.; Barnes, P.R.F.; Randeniya, L.K.; Plumb, I.C.; Grey, I.E.; Horne, M.D.; Glasscock, J.A. Efficiency in solar water splitting using semiconductor electrodes. *Int. J. Hydrogen Energy* **2006**, *31*, 1999–2017. [CrossRef]
6. Tomkiewicz, M.; Fay, H. Photoelectrolysis of water with semiconductors. *Appl. Phys.* **1979**, *18*, 1–28. [CrossRef]
7. Siripala, W.; Ivanovskaya, A.; Jaramillo, T.F.; Baeck, S.H.; Mcfarland, E.W. A Cu_2O/TiO_2 heterojunction thin film cathode for photoelectrocatalysis. *Sol. Energy Mater. Sol. Cells* **2003**, *77*, 229–237. [CrossRef]
8. Guo, Q.; Zhou, C.; Ma, Z.; Ren, Z.; Fan, H.; Yang, X. Elementary photocatalytic chemistry on TiO_2 surfaces. *Chem. Soc. Rev.* **2016**, *45*, 3701–3730. [CrossRef] [PubMed]
9. Schneider, J.; Matsuoka, M.; Takeuchi, M.; Zhang, J.L.; Horiuchi, Y.; Anpo, M.; Bahnemann, D.W. Understanding TiO_2 photocatalysis: Mechanisms and materials. *Chem. Rev.* **2014**, *114*, 9919–9986. [CrossRef] [PubMed]
10. Chang, S.J.; Yang, X.Q.; Sang, Y.; Liu, H. Highly efficient photocatalysts and continuous-flow photocatalytic reactors for degradation of organic pollutants in wastewater. *Chem. Asian J.* **2016**, *11*, 2352–2371. [CrossRef] [PubMed]
11. Fernandez-Domene, R.M.; Lucas-Granados, B.; Garcia-Zamora, C.S.; Garcia-Anton, J. Customized WO_3 nanoplatelets as visible-light photoelectrocatalyst for the degradation of a recalcitrant model organic compound (methyl orange). *J. Photochem. Photobiol. A Chem.* **2018**, *356*, 46–56. [CrossRef]
12. Mehtab, A.; Ingole, P.; Ahmed, J.; Mao, Y.B.; Ahmad, T. Unraveling Quantum Mysteries: Probing the Interplay of CdS Quantum Dots and g-C_3N_4 Nanosheets for Enhanced Photo/Electrocatalytic Hydrogen Evolution. *J. Phys. Chem. C* **2024**, *128*, 85–94. [CrossRef]
13. Hidaka, H.; Shimura, T.; Ajisaka, K.; Horikoshi, S.; Zhao, J.C.; Serpone, N. Photoelectrochemical decomposition of amino acids on a TiO_2/OTE particulate film electrode. *J. Photochem. Photobiol. A Chem.* **1997**, *109*, 165–170. [CrossRef]
14. Rodriguez, J.; Gómez, M.; Lindquist, S.E.; Granqvist, C.G. Photo-electrocatalytic degradation of 4-chlorophenol over sputter deposited Ti oxide films. *Thin Solid Films* **2000**, *360*, 250–255. [CrossRef]
15. Sang, Y.H.; Zhao, Z.H.; Zhao, M.W.; Hao, P.; Leng, Y.H.; Liu, H. From UV to near-infrared, WS_2 nanosheet: A novel photocatalyst for full solar light spectrum photodegradation. *Adv. Mater.* **2014**, *27*, 363–369. [CrossRef] [PubMed]
16. Tian, J.; Leng, Y.H.; Zhao, Z.H.; Xia, Y.; Sang, Y.H.; Hao, P.; Zhan, J.; Li, M.C.; Liu, H. Carbon quantum dots/hydrogenated TiO_2 nanobelt heterostructures and their broad spectrum photocatalytic properties under UV, visible, and near-infrared irradiation. *Nano Energy* **2015**, *11*, 419–427. [CrossRef]
17. Mclaren, A.; Valdes-Solis, T.; Li, G.Q.; Tsang, S.C. Shape and size effects of ZnO nanocrystals on photocatalytic activity. *J. Am. Chem. Soc.* **2009**, *131*, 12540–12541. [CrossRef] [PubMed]
18. Xi, G.C.; Ye, J.H.; Ma, Q.; Su, N.; Bai, H.; Wang, C. In situ growth of metal particles on 3D urchin-like WO_3 nanostructures. *J. Am. Chem. Soc.* **2012**, *134*, 6508–6511. [CrossRef] [PubMed]
19. Chen, J.Z.; Wu, X.J.; Yin, L.S.; Li, B.; Hong, X.; Fan, Z.X.; Chen, B.; Xue, C.; Zhang, H. One-pot synthesis of CdS nanocrystals hybridized with single-layer transition-metal dichalcogenide nanosheets for efficient photocatalytic hydrogen evolution. *Angew. Chem. Int. Ed.* **2015**, *127*, 1226–1230. [CrossRef]

20. Bhira, L.; Essaidi, H.; Belgacem, S.; Couturier, G.; Salardenne, J.; Barreaux, N.; Bernede, J.C. Structural and photoelectrical properties of sprayed β-In_2S_3 thin films. *Phys. Status Solidi* **2000**, *181*, 427–436. [CrossRef]
21. Nah, Y.C.; Paramasivam, I.; Hahn, R.; Shrestha, N.K.; Schmuki, P. Nitrogen doping of nanoporous WO_3 layers by NH_3 treatment for increased visible light photoresponse. *Nanotechnology* **2010**, *21*, 105704. [CrossRef]
22. Liu, Y.; Li, J.; Li, W.Z.; Yang, Y.H.; Li, Y.M.; Chen, Q.Y. Enhancement of the photoelectrochemical performance of WO_3 vertical arrays film for solar water splitting by gadolinium doping. *J. Phys. Chem. C* **2015**, *119*, 14834–14842. [CrossRef]
23. Wang, N.; Wang, D.G.; Li, M.G.; Shi, J.Y.; Li, C. Photoelectrochemical water oxidation on photoanodes fabricated with hexagonal nanoflower and nanoblock WO_3. *Nanoscale* **2014**, *6*, 2061–2066. [CrossRef]
24. Grigioni, I.; Stamplecoskie, K.G.; Selli, E.; Kamat, P.V. Dynamics of photogenerated charge carriers in WO_3/$BiVO_4$ heterojunction photoanodes. *J. Phys. Chem. C* **2015**, *119*, 20792–20800. [CrossRef]
25. Zheng, F.; Lu, H.; Guo, M.; Zhang, M.; Zhen, Q. Hydrothermal preparation of WO_3 nanorod array and ZnO nanosheet array composite structures on FTO substrates with enhanced photocatalytic properties. *J. Mater. Chem. C* **2015**, *3*, 7612–7620. [CrossRef]
26. Fan, X.L.; Gao, B.; Wang, T.; Huang, X.L.; Gong, H.; Xue, H.R.; Guo, H.; Song, L.; Xia, W.; He, J.P. Layered double hydroxide modified WO_3 nanorod arrays for enhanced photoelectrochemical water splitting. *Appl. Catal. A Gen.* **2016**, *528*, 52–58. [CrossRef]
27. Walter, M.G.; Warren, E.L.; Mckone, J.R.; Boettcher, S.W.; Mi, Q.X.; Santori, E.A.; Lewis, N.S. Solar water splitting cells. *Chem. Rev.* **2010**, *110*, 6446–6473. [CrossRef]
28. Chen, H.; Hu, L.F.; Chen, M.; Yan, Y.; Wu, L.M. Nickel–cobalt layered double hydroxide nanosheets for high-performance supercapacitor electrode materials. *Adv. Funct. Mater.* **2013**, *24*, 934–942. [CrossRef]
29. Xu, S.M.; Pan, T.; Dou, Y.B.; Yan, H.; Zhang, S.T.; Ning, F.Y.; Shi, W.Y.; Wei, M. Theoretical and experimental study on $M^{II}M^{III}$-layered double hydroxides as efficient photocatalysts toward oxygen evolution from water. *J. Phys. Chem. C* **2015**, *119*, 18823–18834. [CrossRef]
30. Gao, M.R.; Sheng, W.C.; Zhuang, Z.B.; Fang, Q.R.; Gu, S.; Jiang, J.; Yan, Y.S. Efficient water oxidation using nanostructured α-nickel-hydroxide as an electrocatalyst. *J. Am. Chem. Soc.* **2014**, *136*, 7077–7084. [CrossRef]
31. Gong, M.; Li, Y.G.; Wang, H.L.; Liang, Y.Y.; Wu, J.Z.; Zhou, J.G.; Wang, J.; Regier, T.; Wei, F.; Dai, H.J. An advanced Ni-Fe layered double hydroxide electrocatalyst for water oxidation. *J. Am. Chem. Soc.* **2013**, *135*, 8452–8455. [CrossRef]
32. Lu, Z.Y.; Xu, W.W.; Zhu, W.; Yang, Q.; Lei, X.D.; Liu, J.F.; Li, Y.P.; Sun, X.M.; Duan, X. Three-dimensional NiFe layered double hydroxide film for high-efficiency oxygen evolution reaction. *Chem. Commun.* **2014**, *50*, 6479–6482. [CrossRef]
33. Huang, J.W.; Hu, G.W.; Ding, Y.; Pang, M.C.; Ma, B.C. Mn-doping and NiFe layered double hydroxide coating: Effective approaches to enhancing the performance of α-Fe_2O_3 in photoelectrochemical water oxidation. *J. Catal.* **2016**, *340*, 261–269. [CrossRef]
34. Luo, J.S.; Im, J.H.; Mayer, M.T.; Schreier, M.; Nazeeruddi, M.K.; Park, N.G.; Tilley, S.D.; Fan, H.J.; Grätzel, M. Water photolysis at 12.3% efficiency via perovskite photovoltaics and Earth-abundant catalysts. *Science* **2014**, *345*, 1593–1596. [CrossRef]
35. Akinterinwa, O.; Cirino, P.C. Heterologous expression of xylulokinase from Pichia stipitis enables high levels of xylitol production by engineered Escherichia coli growing on xylose. *Metab. Eng.* **2009**, *11*, 48–55. [CrossRef]
36. Nair, N.U.; Zhao, H.M. Selective reduction of xylose to xylitol from a mixture of hemicellulosic sugars. *Metab. Eng.* **2010**, *12*, 462–468. [CrossRef]
37. Parachin, N.S.; Bergdahl, B.; van Niel, E.W.J.; Gorwa-Grauslund, M.F. Kinetic modelling reveals current limitations in the production of ethanol from xylose by recombinant Saccharomyces cerevisiae. *Metab. Eng.* **2011**, *13*, 508–517. [CrossRef]
38. Liu, H.W.; Valdehuesa, K.N.G.; Nisola, G.M.; Ramos, K.R.M.; Chung, W.J. High yield production of D-xylonic acid from D-xylose using engineered *Escherichia coli*. *Bioresour. Technol.* **2012**, *115*, 244–248. [CrossRef]
39. Cañete-Rodríguez, A.M.; Santos-Dueñas, I.M.; Jiménez-Hornero, J.E.; Ehrenreich, A.; Liebl, W.; García-García, I. Gluconic acid: Properties, production methods and applications—An excellent opportunity for agro-industrial by-products and waste bio-valorization. *Process Biochem.* **2016**, *51*, 11891–11903. [CrossRef]
40. Toivari, M.; Nygård, Y.; Kumpula, E.P.; Vehkomäki, M.L.; Benčina, M.; Valkonen, M.; Maaheimo, H.; Andberg, M.; Koivula, A.; Ruohonen, L.; et al. Metabolic engineering of saccharomyces cerevisiae for bioconversion of d-xylose to d-xylonate. *Metab. Eng.* **2012**, *14*, 427–436. [CrossRef]
41. Chen, L.; Huang, Y.M.; Zou, R.; Ma, J.L.; Yang, Y.Y.; Li, T.Z.; Li, M.S.; Hao, Q.; Xie, H.B.; Peng, X.W. Regulating TiO_2/MXenes Catalysts to Promote Photocatalytic Performance of Highly Selective Oxidation of D-xylose. *Green Chem.* **2021**, *23*, 1382–1388. [CrossRef]
42. Li, M.S.; Zhong, L.X.; Chen, W.; Huang, Y.M.; Chen, Z.X.; Xiao, D.Q.; Zou, R.; Chen, L.; Hao, Q.; Liu, Z.H.; et al. Regulating the Electron-Hole Separation to Promote Selective Oxidation of Biomass using ZnS@Bi_2S_3 Nanosheet Catalyst. *Appl. Catal. B Environ.* **2021**, *292*, 120180. [CrossRef]
43. Rafaïdeen, T.; Baranton, S.; Coutanceau, C. Highly efficient and selective electrooxidation of glucose and xylose in alkaline medium at carbon supported alloyed PdAu nanocatalysts. *Appl. Catal. B Environ.* **2019**, *243*, 641–656. [CrossRef]
44. Mirescu, A.; Prüße, U. A new environmental friendly method for the preparation of sugar acids via catalytic oxidation on gold catalysts. *Appl. Catal. B Environ.* **2007**, *70*, 644–652. [CrossRef]
45. Coutanceau, C.; Zalineeva, A.; Baranton, S.; Simoes, M. Modification of palladium surfaces by bismuth adatoms or clusters: Effect on electrochemical activity and selectivity towards polyol electrooxidation. *Int. J Hydrogen Energy* **2014**, *39*, 15877–15886. [CrossRef]

46. González Cobos, J.; Baranton, S.; Coutanceau, C. Development of bismuth-modified PtPd nanocatalysts for the electrochemical reforming of polyols into hydrogen and value-added chemicals. *Chemelectrochem* **2016**, *3*, 1694–1704. [CrossRef]
47. Simões, M.; Baranton, S.; Coutanceau, C. Electrochemical valorisation of glycerol. *Chemsuschem* **2012**, *5*, 2106–2124. [CrossRef]
48. Song, D.D.; Cui, P.; Zhao, X.; Li, M.C.; Chu, L.H.; Wang, T.Y.; Jiang, B. Tungsten trioxide nanoplate array supported platinum as a highly efficient counter electrode for dye-sensitized solar cells. *Nanoscale* **2015**, *7*, 5712–5718. [CrossRef]
49. Sim, Y.M.; Kim, J.; Seong, M.J. Simple synthesis of ultra-high quality In_2S_3 thin films on InAs substrates. *J. Alloys Compd.* **2016**, *685*, 518–522. [CrossRef]
50. Rengaraj, S.; Venkataraj, S.; Tai, C.W.; Kim, Y.H.; Repo, E.; Sillanpää, M. Self-assembled mesoporous hierarchical-like In_2S_3 hollow microspheres composed of nanofibers and nanosheets and their photocatalytic activity. *Langmuir* **2011**, *27*, 5534–5541. [CrossRef]
51. Shen, J.F.; Yan, B.; Shi, M.; Ma, H.W.; Li, N.; Ye, M.X. One step hydrothermal synthesis of TiO_2-reduced graphene oxide sheets. *J. Mater. Chem.* **2011**, *21*, 3415–3421. [CrossRef]
52. Mcintyre, N.S.; Zetaruk, D.G. X-ray photoelectron spectroscopic studies of iron oxides. *Anal. Chem.* **1977**, *49*, 1521–1529. [CrossRef]
53. Boningari, T.; Ettireddy, P.R.; Somogyvari, A.; Liu, Y.; Vorontsov, A.; Mcdonald, C.A.; Smirniotis, P.G. Influence of elevated surface texture hydrated titania on Ce-doped Mn/TiO_2 catalysts for the low-temperature SCR of NO_x under oxygen-rich conditions. *J. Catal.* **2015**, *325*, 145–155. [CrossRef]
54. Du, Y.Y.; Wang, Q.; Liang, X.; He, Y.F.; Feng, J.T.; Li, D.Q. Hydrotalcite-like MgMnTi non-precious-metal catalyst for solvent-free selective oxidation of alcohols. *J. Catal.* **2015**, *331*, 154–161. [CrossRef]
55. Qiu, W.M.; Xu, M.S.; Yang, X.; Chen, F.; Nan, Y.X.; Zhang, J.L.; Iwai, H.; Chen, H.Z. Biomolecule-assisted hydrothermal synthesis of In_2S_3 porous films and enhanced photocatalytic properties. *J. Mater. Chem.* **2011**, *21*, 13327–13333. [CrossRef]
56. Zhang, X.; Li, X.H.; Shao, C.L.; Li, J.H.; Zhang, M.Y.; Zhang, P.; Wang, K.X.; Lu, N.; Liu, Y.C. One-dimensional hierarchical heterostructures of In_2S_3 nanosheets on electrospun TiO_2 nanofibers with enhanced visible photocatalytic activity. *J. Hazard. Mater.* **2013**, *260*, 892–900. [CrossRef] [PubMed]
57. Zhang, L.W.; Reisner, E.; Baumberg, J.J. Al-doped ZnO inverse opal networks as efficient electron collectors in $BiVO_4$ photoanodes for solar water oxidation. *Environ. Sci. Technol.* **2014**, *7*, 1402–1408. [CrossRef]
58. Seabold, J.A.; Choi, K.S. Efficient and stable photo-oxidation of water by a bismuth vanadate photoanode coupled with an iron oxyhydroxide oxygen evolution catalyst. *J. Am. Chem. Soc.* **2012**, *134*, 2186–2192. [CrossRef] [PubMed]
59. Krol, R.V.D. Principles of Photoelectrochemical Cells. In *Photoelectrochemical Hydrogen Production*; Springer: New York, NY, USA, 2012.
60. Huang, Y.; Yu, Y.F.; Xin, Y.N.; Meng, N.N.; Yu, Y.; Zheng, B. Promoting charge carrier utilization by integrating layered double hydroxide nanosheet arrays with porous $BiVO_4$ photoanode for efficient photoelectrochemical water splitting. *Sci. China Mater.* **2017**, *60*, 193–207. [CrossRef]
61. Wang, J.F.; Wu, D.D.; Liu, Q.Q.; Zhang, X.F.; Lan, X.Q.; Song, H. Determination of xylose content in corncob hydrolyzate by phloroglucinol method. *J. Anhui Agric. Sci.* **2011**, *39*, 13542–13544. [CrossRef]

Disclaimer/Publisher's Note: The statements, opinions and data contained in all publications are solely those of the individual author(s) and contributor(s) and not of MDPI and/or the editor(s). MDPI and/or the editor(s) disclaim responsibility for any injury to people or property resulting from any ideas, methods, instructions or products referred to in the content.